

Radial Alignment of Carbon Nanotubes via Dead-End Filtration

Christian Rust, Elias Schill, Oisín Garrity, Manuel Spari, Han Li, Andreas Bacher, Markus Guttman, Stephanie Reich, and Benjamin S. Flavel*

Dead-end filtration is a facile method to globally align single wall carbon nanotubes (SWCNTs) in large area films with a 2D order parameter, S_{2D} , approaching unity. Uniaxial alignment has been achieved using pristine and hot-embossed membranes but more sophisticated geometries have yet to be investigated. In this work, three different patterns with radial symmetry and an area of 3.8 cm² are created. Two of these patterns are replicated by the filtered SWCNTs and S_{2D} values of ≈ 0.85 are obtained. Each of the radially aligned SWCNT films is characterized by scanning cross-polarized microscopy in reflectance and laser imaging in transmittance with linear, radial, and azimuthal polarized light fields. The former is used to define a novel indicator akin to the 2D order parameter using Malu's law, yielding 0.82 for the respective film. The films are then transferred to a flexible printed circuit board and terminal two-probe electrical measurements are conducted to explore the potential of those new alignment geometries.

applications, including but not limited to energy capture^[1] and storage,^[2] and communication^[3] and microsized light sources.^[4] SWCNTs are a quasi 1D object with exceptional and highly anisotropic physical properties.^[5] The diameter of an SWCNT is defined by its chiral indices (n, m) classifying the SWCNT as either semiconducting (s) or metallic (m) and determine the spectral position of absorption bands in the ultraviolet, visible or infrared.^[6] In order to make use of, or in many cases overcome, the inherent anisotropy of an SWCNT,^[7] it is necessary to develop methods to control the orientation not only of a single SWCNT, but entire thin films thereof spanning over multiple square centimeters. Alignment techniques that rely on as-grown

1. Introduction

Single wall carbon nanotubes (SWCN) have been envisioned to find use in many next generation photonic and electronic


CNT forests^[8] are generally unfavorable for device applications despite their simplicity and large area, due to difficulties in controlling the growth of the SWCNTs with the required chiral purity. In contrast, dispersion based techniques allow for length sorting,^[9] removal of unreacted carbon and catalysts,^[10] as well as chiral enrichment prior to alignment,^[11] but they are often limited by the attainable area of the film.^[12] Nevertheless, many of these techniques have been shown to afford a high degree of alignment.^[11a,13] However, in recent developments in the field, Jinkins et al. utilized the interface between water and an organic s-SWCNT ink to obtain an aligned film with an area of 6.25 cm²,^[14] and Rust et al. used dead-end filtration of aqueous dispersions to obtain an area of 3.8 cm² with an S_{2D} value of 0.85.^[15]

C. Rust, E. Schill, M. Spari, H. Li, B. S. Flavel
Institute of Nanotechnology
Karlsruhe Institute of Technology
Hermann-von-Helmholtz Platz 1
76344 Eggenstein-Leopoldshafen, Germany
E-mail: benjamin.flavel@kit.edu

C. Rust
Institute of Materials Science
Technische Universität Darmstadt
Alarich-Weiss-Straße 2, 64287 Darmstadt, Germany

O. Garrity, S. Reich
Institute of Experimental Physics
Freie Universität Berlin
Arnimallee 14, 14195 Berlin, Germany

A. Bacher, M. Guttman
Institute of Microstructure Technology
Karlsruhe Institute of Technology
Hermann-von-Helmholtz-Platz 1
76344 Eggenstein-Leopoldshafen, Germany

 The ORCID identification number(s) for the author(s) of this article can be found under <https://doi.org/10.1002/smll.202207684>.

© 2023 The Authors. Small published by Wiley-VCH GmbH. This is an open access article under the terms of the Creative Commons Attribution License, which permits use, distribution and reproduction in any medium, provided the original work is properly cited.

The use of dead-end filtration,^[16] to obtain nematically ordered films of SWCNTs began with Dan et al.^[17] and King and Panchapakesan^[18] who observed the formation single domains (several μm^2 in size) when aqueous dispersions of SWCNTs were filtered onto polycarbonate track-etched (PCTE) and mixed cellulose ester membranes, and this, despite the use of SWCNT concentrations (45 and 0.01 mg mL⁻¹) being well below the required concentration for liquid crystal formation (1.5 g mL⁻¹).^[19] In 2016, He et al. then demonstrated using even more dilute dispersions of SWCNTs (10 $\mu\text{g mL}^{-1}$), that it was possible to produce an SWCNT film that was globally aligned by carefully adjusting the flowrates during filtration.^[15c] In their work the term global alignment was coined to describe a film that is large area ($>\text{cm}^2$) and with a single alignment direction, but the mechanism that drives this uniform alignment is

DOI: 10.1002/smll.202207684

still the subject of debate. He et al. focused on electric charges on the membrane, which repel the SWCNTs during filtration and suggested that they are able to perform collective in-plane rotations above its surface.^[15c] Walker et al. suggested that these surface charges must also be directional and reported an increase of the S_{2D} order parameter for films made with intentionally unidirectional tribo-charged membranes.^[15b,20] Alternatively, Komatsu et al. investigated surface grooves in the PCTE membranes used for this technique^[15,20,21] and showed a significant increase in alignment by artificially adding grooves with hot-embossing (HE) process.^[21] Custom-made setups by Walker et al.^[15b] and Rust et al.^[15a] have also allowed for reproducible studies of various filtration conditions required for alignment. Additionally, Rust et al. suggested that alignment on pristine membranes is a result of shear flow on the membrane surface, as large aligned regions could be achieved despite using SWCNTs dispersed with positively charged cetrimonium bromide and negatively charged sodium deoxycholate (DOC). However, using hot-embossed membranes, resulted in a change of filtration mode (intermediate fouling to cake filtration) and was accompanied by SWCNTs predominately adhering to the artificially created edges, implying that the mechanism varies with the modification of the membrane used.^[15a]

Unidirectional alignment of SWCNTs is an impressive step forward in the control and self-assembly of nanomaterials and has been already used to fabricate linear polarizers for the fast growing field of terahertz spectroscopy^[22] in order to replace the inflexible, brittle wire grid polarizers, which require high precision fabrication processes^[23] and are exhibiting low extinction ratios compared to their infrared/vis counterparts.^[24] Recently, Baydin et al. showed the existence of a “magic” angle (30°) between the THz pulse and an aligned SWCNT thin film ($t \approx 45$ nm) made with the filtration method, which rotated the polarization by exactly 90°, due to the high anisotropy of the optical constants of the film and SWCNTs.^[25] However, to our knowledge, radial polarizers were only assembled by an arrangement of multiple wire-grids to date, rather than using a continuous structure,^[26] even though there is a plethora of applications benefitting from this distinctive polarization. These applications involve optical tweezers and cold atom trapping using hollow beams,^[27] ultra-compact electron accelerators,^[28] chiral spectroscopy with spatiotemporal resolution for spintronics,^[29] as well as fluorescence^[30] and molecular^[31] orientation microscopy. In other wavelength ranges, radial aligned SWCNTs could find use cases as optical limiters for sensors and eyesight against radial polarized lasers,^[32] due to their high absorption in the infrared/vis range, ($\lambda \approx 400$ –800 nm) as well as photomasks in the extreme UV wavelength range ($\lambda \approx 10$ nm).^[33] Outside of optics, aligned SWCNTs have been considered for thermal management, in which radial aligned SWCNTs would offer the possibility of an even distribution of heat from the center.^[34]

In general, optical polarization is achieved by polarization dependent absorption (dichroism) and birefringence, which are a consequence of orientation-dependent differences in refractive indices and is observed in anisotropic, non-spherical objects such as SWCNTs,^[35] or structured materials like globally aligned thin films thereof.^[15a] The latter is described by, electromagnetic radiation entering an anisotropic material at

an axis not coinciding with the optical axis splitting into an ordinary and extraordinary ray with their polarization being mutual perpendicular, as the velocities differ based on the path taken by the extraordinary ray. The degree of anisotropy of the material is commonly characterized by cross polarized microscope (CPM) and an evaluation of the contrast between the combined intensity of both rays at the extinction angle of the sample $\left(\theta = 0 + n \frac{\pi}{2}\right)$ and at the brightest angle $\left(\theta = \frac{\pi}{2} + n \frac{\pi}{2}\right)$, following Malu’s law.^[36] In this work, we fabricated three nickel shims (stamps) with rotational symmetric patterns and used a custom HE setup^[37] to imprint these into an 80 nm pore size polyvinylpyrrolidone (PVP) coated PCTE membrane. In this way we are able to demonstrate alignment angles of 0°–360° within a single film and confirm it via CPM, Raman spectroscopy, laser transmittance and electrical terminal two probe resistance measurements.

2. Results and Discussion

Electron beam lithography was used to prepare the polymer masks used for electroforming of the custom nickel shims. A schematic of each and corresponding AFM topographies are shown in **Figure 1**. These had radially symmetric designs and will hereafter be referred to as the a) spoke (SP), b) cake (CA), and c) herringbone (HB) patterns. All shims had an unstructured circular region at their center with a diameter of 2 mm and an outer perimeter of 22 mm. The outer perimeter was set to match our custom microfluidic setup and afforded a total embossed area of 3.81 cm².^[15a] As the name suggests the SP pattern consisted of 5236 spokes extending radially from the center. These had a constant width and pitch of $w_{SP \text{ shim int.}} = 600$ nm on the interior (int.) of the shim. Upon extension toward the exterior (ext.), the spoke width was held constant ($w_{SP \text{ shim ext.}} = 560$ nm) and the pitch was linearly increased to ≈ 13 μm . A variation in height of 10 nm was found between the interior ($h_{SP \text{ shim int.}} = 170$ nm) and exterior ($h_{SP \text{ shim ext.}} = 180$ nm) of the shim, due to inhomogeneities in the resist height during master fabrication via spin coating. The CA pattern was similar to the SP pattern except that now the width and pitch of the bars were increased linearly from the center to the outer perimeter of the shim. Once again, there were 5236 bars in total and the width and pitch of these was $w_{CA \text{ shim int.}} = 560$ nm at the interior. On the exterior of the shim the pitch and width of the spokes was $w_{CA \text{ shim ext.}} = 6.8$ μm . No variation in height was found between the interior and exterior of the shim ($h_{CA \text{ shim int.}} = h_{CA \text{ shim ext.}} = 160$ nm). The HB pattern was obtained by exchanging the straight spokes of the SP pattern with herringbones consisting of bars orientated 45° to the radial direction and rotated by 90° every 1.45 μm . The number of bars was consistent with the other shims and the width of these was held constant between the interior and exterior of the shim ($w_{HB \text{ shim int.}} = 1.4$ μm , $w_{HB \text{ shim ext.}} = 1.35$ μm). Like the SP pattern, a variation in height of 10 nm was found between the interior ($h_{HB \text{ shim int.}} = 155$ nm) and exterior ($h_{HB \text{ shim ext.}} = 165$ nm) of the shim.

Following our previous protocol,^[15a,21] 20 kN of force and a temperature of 120 °C were used to imprint these patterns

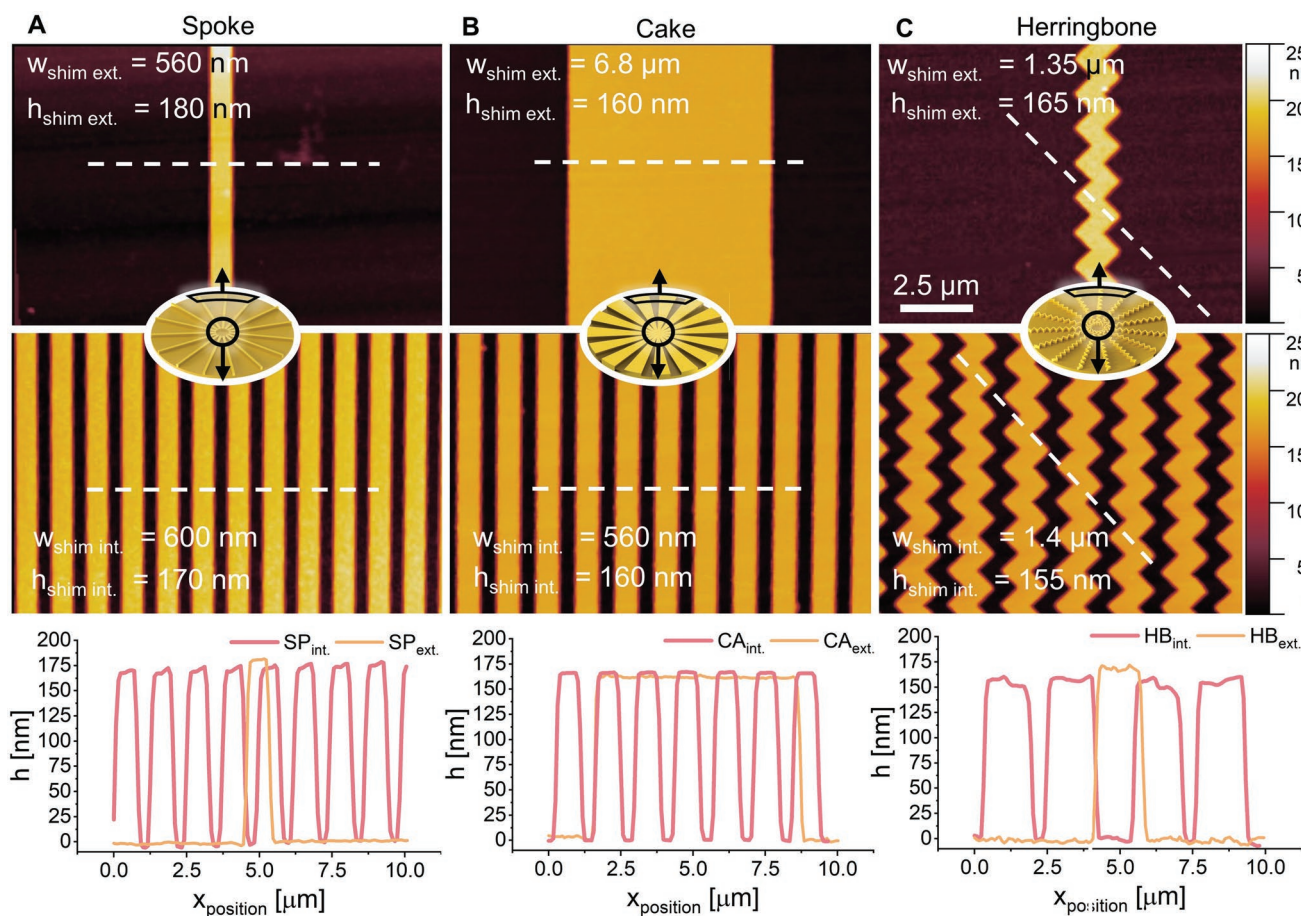


Figure 1. Schematics and AFM topographies of the shim structures used for hot-embossing of the PCTE membranes. These had a A) spoke (SP), B) cake (CA), and C) herringbone (HB) patterns, which are represented by images taken at the interior and exterior of the shim and corresponding line scans along the white dashed lines, used to determine the average width and height of those structures.

into 80 nm pore size PCTE membranes ($t_{\text{membrane}} = 25 \mu\text{m}$, $\epsilon_{\text{porosity}} = 6 \times 10^8 \text{ cm}^{-2}$). The shim was in contact with the membrane for ≈ 10 min after heating up by $95 \text{ }^\circ\text{C min}^{-1}$, before the membrane was removed from the HE setup at $40 \text{ }^\circ\text{C}$ using an average cooling rate of $4 \text{ }^\circ\text{C min}^{-1}$.^[15a] Forces > 20 kN resulted in the membranes appearing transparent to the eye in some locations and were accompanied by a closure of the pores. Consequently, when SWCNTs were filtered through these membranes only the pores in the less deformed regions were open and a discontinuous SWCNT film was obtained. Lower loadings (16 kN) led to partial replication of the patterns in the membrane. AFM-Topographies of the membranes after HE are shown in Figure S1, Supporting Information. In all cases, it can be seen that the shims were reproduced laterally with an accuracy of ± 45 nm. The CA pattern was found to impart an even imprint on the membrane with a ≈ 10 nm difference between the height of the structures on the interior ($h_{\text{CA HE int.}} = 22$ nm) compared to the exterior ($h_{\text{CA HE ext.}} = 35$ nm) of the membrane. For the SP and HB pattern the structures were found to be significantly taller on the exterior ($h_{\text{SP HE ext.}} = 145$ nm, $h_{\text{HB HE ext.}} = 145$ nm) of the membrane compared to the interior ($h_{\text{SP HE int.}} = 20$ nm, $h_{\text{HB HE int.}} = 70$ nm). This is due to the higher density of structures in the center compared to the outer

circumference and thus lower deformation in the middle compared to the circumference. On the contrary, for the CA pattern the spacing and width of the spokes are equal across the whole shim and this leads to a constant deformation. Comparing the height of the imprints to the shim height ($h_{\text{SP shim avg}} = 175$ nm, $h_{\text{HB shim avg}} = 160$ nm), also indicates how higher applied forces lead to the entire shim surface contacting the membrane and a closure of additional pores.

Electric arc (EA) synthesized SWCNTs were dispersed by 1 wt% DOC in water and concentrated to $800 \mu\text{g mL}^{-1}$. This concentration of SWCNTs was required in order to reach the required low surfactant concentration and mass of SWCNTs by dilution with water ($8 \mu\text{g mL}^{-1}$ EA-SWCNTs, 0.04 wt% DOC). The filtration parameters were consistent with those used previously for uniaxially structured membranes; 1.25 mL of the diluted SWCNT dispersion was filtered at $100 \mu\text{L min}^{-1}$ followed by a pushing step of $500 \mu\text{L min}^{-1}$ for the last 0.75 mL^[15a] The measured filtration resistance, $R_{\text{cp} + \text{b}}$, which can be understood as the increase in resistance due to the accumulation of SWCNTs on the membrane ($R_{\text{tot}} - R_{\text{m}}$),^[38] showed an instantaneous linear increase over the volume filtered for all membranes except the ones imprinted with the HB pattern, Figure S2, Supporting Information. A linear increase in

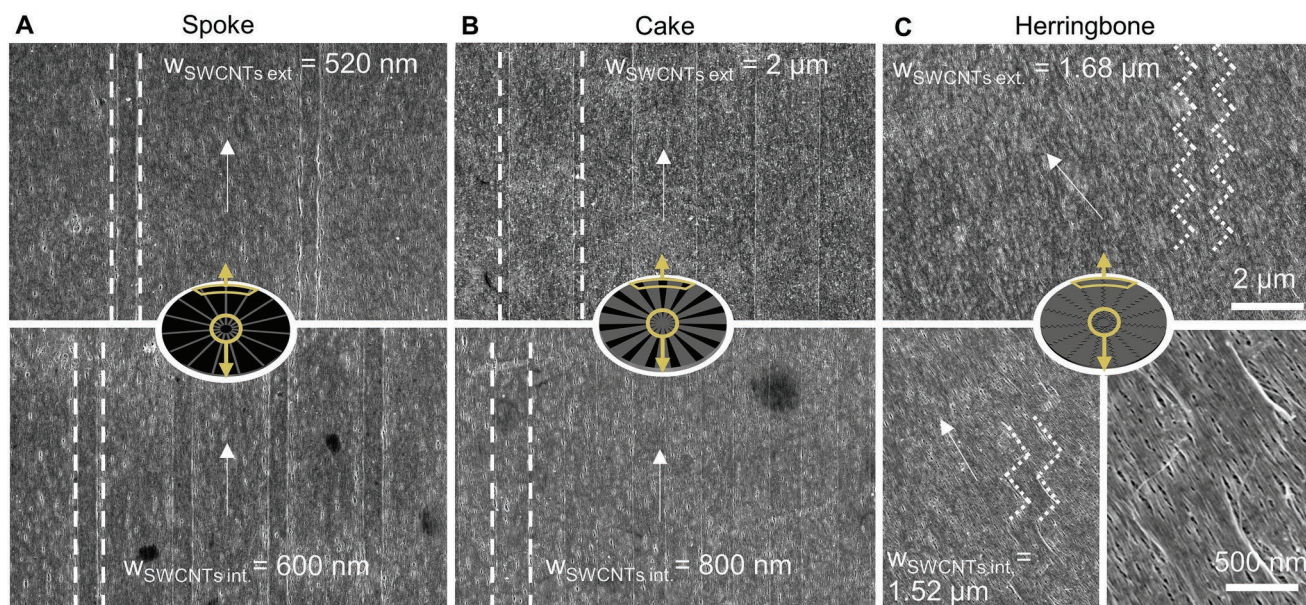


Figure 2. Schematic representation and SEM images of SWCNT films transferred to an fPCB (polyamide with gold contacts) made from membranes with A) spoke (SP), B) cake (CA), and C) herringbone (HB) patterns. The alignment direction is indicated by an arrow to guide the eye.

filtration resistance is consistent with cake filtration without an initial concentration polarization (CP) regime also found for axial patterned membranes and can be interpreted as the SWCNTs not gathering above the membrane, but rather being directly adsorbed at the edges of the hot-embossed patterns.^[15a] We thus suspect, that the alignment mechanisms discussed for uniaxial alignment should also apply here.^[15,39] For the HB pattern, an intermediate blocking could be observed, which has been observed previously using pristine membranes forming globally aligned films.^[15a]

After filtration, the SWCNT films were transferred to either glass substrates or flexible printed circuit boards (fPCBs). The latter allowed for scanning electron microscopy (SEM) imaging and electrical characterization of the film. The films were imaged close to the ground contact in the center ($r = 1.3$ mm) and the cake-shaped channel contacts in the outer perimeter being another 2 mm further outward. It can be seen in **Figure 2**, that the SP and CA patterns were well replicated by the SWCNTs at the center and circumference of the film. And in fact, for the SP and CA-patterns, the SWCNT alignment followed the templates, leading to constant bar widths for the SP pattern ($w_{SP\ SWCNTs\ int.} = 600$ nm, $w_{SP\ SWCNTs\ ext.} = 520$ nm) and increasing bar widths for the CA pattern depending on the distance to the middle ($w_{CA\ SWCNTs\ int.} = 800$ nm, $w_{CA\ SWCNTs\ ext.} = 2000$ nm). Higher magnified images can be found in Figure S3, Supporting Information. For the HB pattern the SWCNTs did not mimic the pattern directly, but rather follow an average direction given by the alternating bars. Nevertheless, it was still possible to identify the original pattern due to a small height difference in the film. The HB pattern does thereby provide an insight into the limitations of the HE method for SWCNT alignment and the associated mechanism thereof as the SWCNTs ($l = 691 \pm 471$ nm)^[15a] are not able to mimic abrupt directional changes (90°) on a comparable length scale (1.45 μ m). Furthermore, the fact that the SWCNTs are aligned in a general

direction given by the radial symmetry, confirms the hypothesis that SWCNTs align by a tangential flow created by grooves present on the surface of the membrane,^[15a] rather than charges influencing the positioning of the SWCNTs directly.^[15b,c,20] This might also explain the difference in fouling types observed for the CA and SP patterned membranes in contrast to the herringbone patterned ones.

To further characterize the radial alignment in the SP and CA films, scanning cross-polarized microscopy (SCPM) in reflectance was used to measure the films transferred to glass. Alternative to SEM, this enabled a macroscale characterization of the film by stitching multiple $5 \times$ -magnified micrographs into a single image/map. Full maps were recorded under rotation of the SWCNT film in 10° intervals and compiled into a graphics interchange format (GIF) movie that is available in the electronic supporting information (Reflectance_Cake.gif). Representative images for the CA film at 60° intervals are shown in **Figure 3A**. Two important observations can be made from the cross polarized images; a) a flower-like light pattern of bright and dark regions is obtained and b) this pattern remains invariant to sample rotation. The latter provides a confirmation of the homogeneity of the radial pattern and the former is a result of the changing SWCNT orientation relative to the polarization of the incident light. In order to analyze the observed light pattern, representative images of the CA and SP films are evaluated by the accumulated intensity with respect to the film angle φ and the film radius r , displayed in Figure S4, Supporting Information. Thereby the film angle φ is starting at the 12 o'clock position and increases with a clockwise rotation, while the origin of the film radius r is placed at the center of the film and increases with the distance to the middle. The unaligned region in the middle of the film ($r < 1$ mm) and the lesser aligned outer perimeter close to the filtration cylinder wall ($r > 75$ mm) were excluded, resulting in the film angle φ resolved intensity plots shown in Figure 3B. The intensity distribution

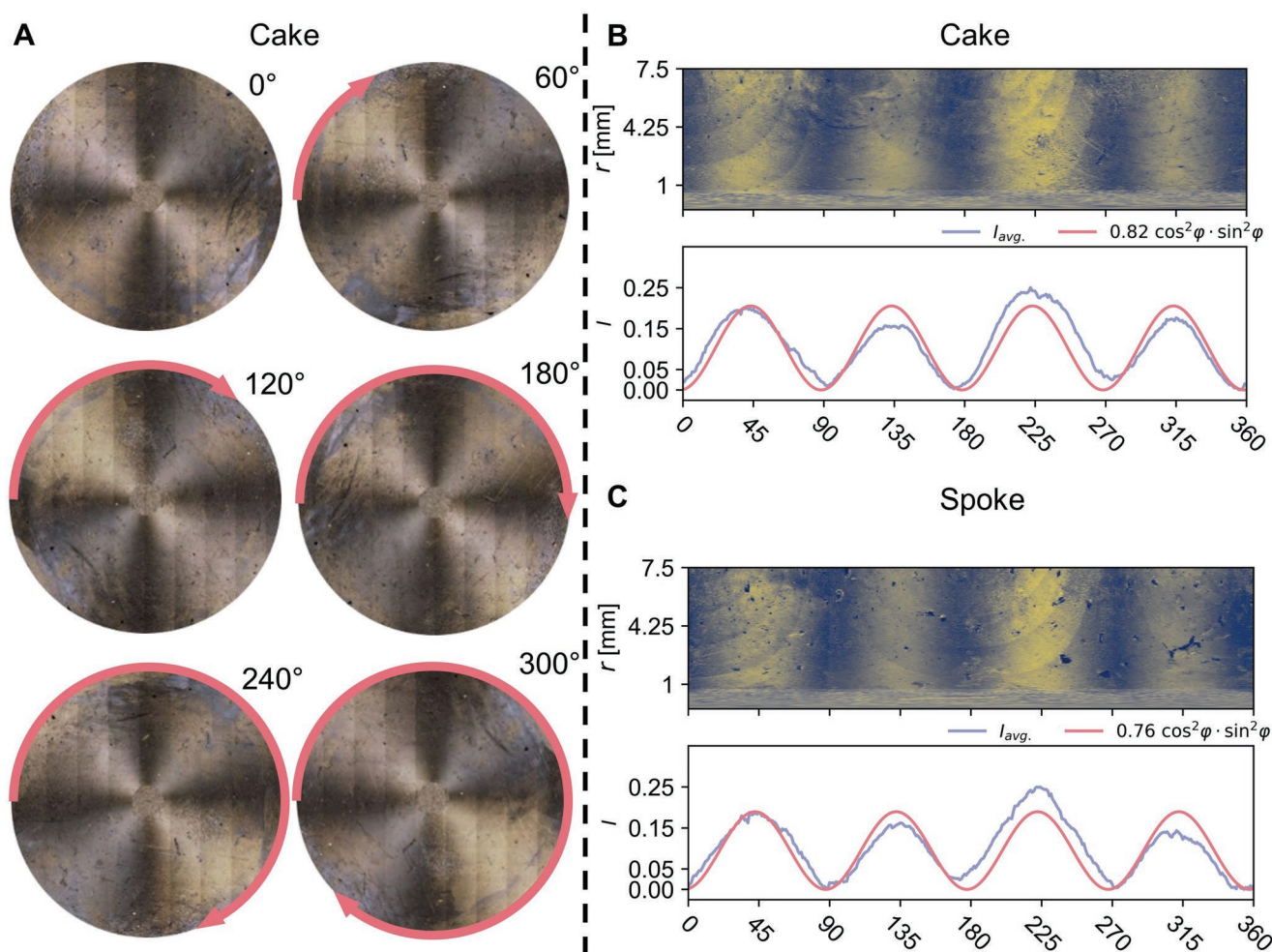


Figure 3. A) Scanning cross polarized microscopy of an SWCNT film created from the CA pattern at 60° intervals of sample rotation, showing the flower-light pattern. The incident polarized light was aligned with the 12 o'clock position of the film. B) The accumulated intensity ignoring the unstructured center ($r < 1$ mm) as well as the lesser aligned outer region ($r > 7.5$ mm) for the B) SP and C) CA patterns (cf. Figure S4, Supporting Information) could be fitted with $I = I_0 \cos^2(\varphi) \sin^2(\varphi)$ derived from Malu's law.^[36]

$I(\varphi)$ can be compared to linear polarized light I_0 passing a linear polarizer grating at an angle φ and thus Malu's law^[36] can be used to derive $I = I_0 \cos^2(\varphi) \sin^2(\varphi)$ (supporting information and also plotted in Figure 3B). The high intensities are thereby found at $\varphi = 0 + n \frac{\pi}{2}$ and the low intensities at $\varphi = \frac{\pi}{2} + n \frac{\pi}{2}$, for $n \in \mathbb{N}$. To test this hypothesis, the intensity of the images is averaged over the radius for every film angle φ and the lowest value obtained is set to 0. The maximum value of the average intensity obtained over the radius is then set to 0.25, so it matches the maximum value of I that can be obtained for $I_0 = 1$, which would correspond to a perfect polarizer and the other values are then normalized accordingly. Fitting the formula to the averaged data yielded, $I_{0\text{ CA}} = 0.82 \pm 0.02$ and $I_{0\text{ SP}} = 0.76 \pm 0.02$, which we propose to use as indicator to assess large scale alignment of a film using a CPM like the S_{2D} order parameter ranging from 0 to 1.

Similar experiments were also performed in transmission with linearly polarized light and once again a GIF movie under 360° sample rotation of the CA pattern can be found in

the electronic supporting information: Transmittance_Cake.gif. A schematic representation of the optical setup used to record those images can be found in Figure S5, Supporting Information.

A supercontinuum laser was used to produce an excitation wavelength of 650 nm which was then guided through two convex, achromatic lenses to expand the beam to cover the area of the CNT film on a glass substrate. After transmission through the film, the light was then guided through two more achromatic lenses to shrink the beam so that it could be fully absorbed by a beam profiler. A cross-polarized measurement was performed by linearly polarizing the incident beam, transmitting it through the film, passing the transmitted beam through an analyzer that is polarized 90° to the incident beam, and finally recording the intensity. The gif then created, consists of intensity images recorded every 10° of film rotation. Once again, a flower pattern of bright and dark regions was obtained, Figure 4A. However, importantly, because this pattern also appears in transmission it indicates that there is a high level of SWCNT alignment within the film and not just on the

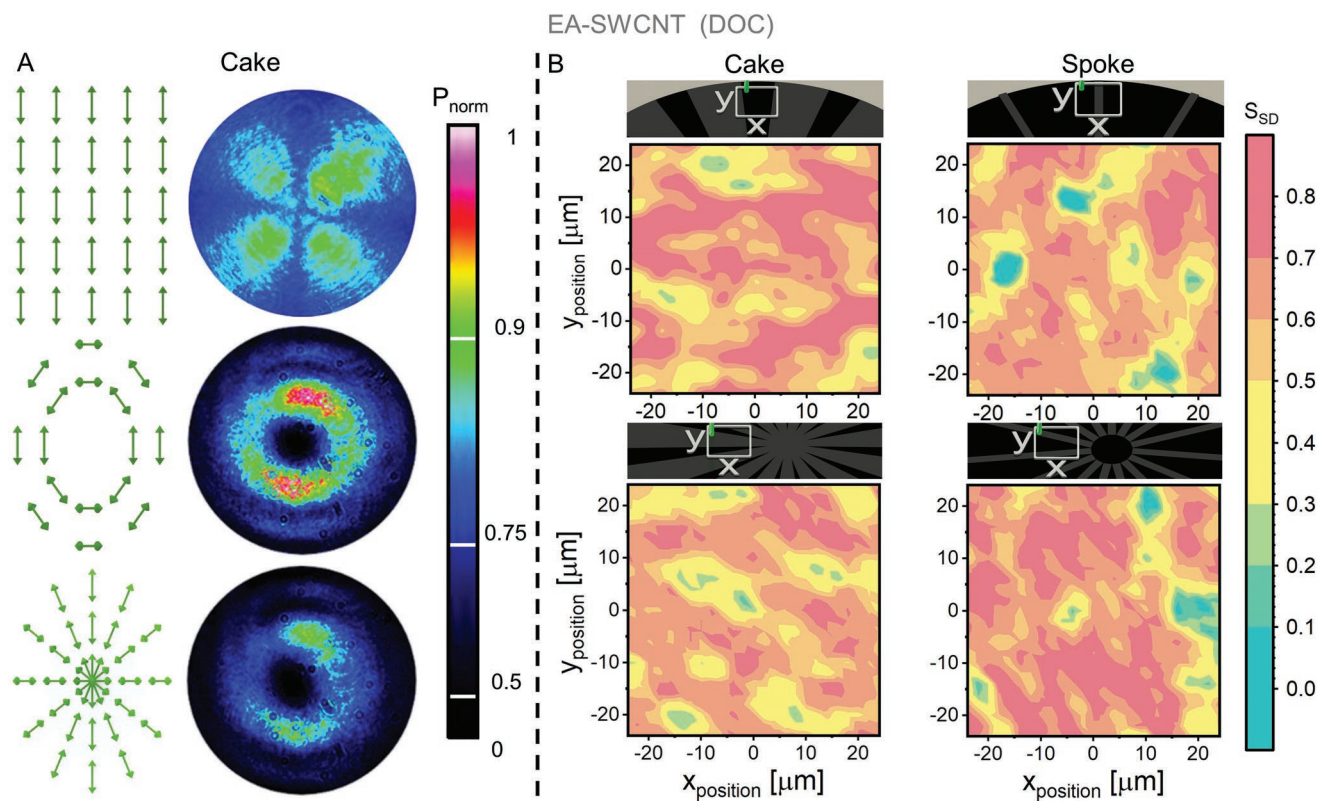


Figure 4. A) Laser transmittance measurements made with linear, azimuthal, and radial polarized light and a CA patterned film. The linear polarization creates a flower like pattern similar to the CPM images shown above. On the contrary, for the latter polarizations the beam profiles do not change, but an increase in absorption can be observed for the radial polarization coinciding with the alignment of the SWCNTs. B) Raman mapping showing the order parameter S_{2D} measured with a 532 nm laser on the films interior (bottom) and exterior (top).

upper-most surface as the film thickness is ≈ 60 nm given by the amount of SWCNTs used (16 μg).^[15a] The homogeneity of the alignment was further verified with the use of azimuthal and radially polarized light fields and is depicted in Figure 4B for a CA film and in Figure S6, Supporting Information for an SP film. Slight variations of the power measured, might be due to the alignment of the optical elements in the measurement setup and/or due to minor differences in deposited SWCNT mass over the whole membrane area.

These measurements rely upon the difference in absorption cross section parallel (larger) and perpendicular (smaller) to the SWCNTs axis.^[35] For azimuthal polarized light, the electric field is perpendicular to the axis of the SWCNTs and for radially polarized light it is parallel. This leads to a difference in the transmitted intensity for the two different light fields for a laser power measured right before the films of 9.1 μW (SP pattern: 5.55 μW (azimuthal) versus 4.48 μW (radial); CA pattern: 6.31 μW (azimuthal) versus 4.51 μW (radial)).

Resonant Raman maps measured with a 532 nm laser excitation over an area of 576 μm^2 in the center and circumference of the film were used to evaluate the 2D alignment parameter S_{2D} , following the method of Zamora-Ledezma et al.,^[13c] Figure 4C. The intensities of the G^+ mode ($\approx 1590 \pm 3$ cm^{-1}) in the different polarization configurations (I_{HH} , I_{VV} and I_{VH}) can be found in Figures S7 and S8, Supporting Information. For calculation of S_{2D} , a dichroic ratio $\Delta(532$ nm) = 1.55 was used.^[15a] The S_{2D} value measured in the middle and perimeter of the films were 0.82

and 0.78 for the SP pattern and 0.82 and 0.85 for the CA pattern, respectively. These values are comparable to those reported for globally aligned SWCNTs films via the filtration method without HE using EA-SWCNTs (S_{3D} He et al. = 0.96,^[15c] S_{2D} Walker et al. = 0.9,^[15b] S_{2D} Rust et al. = 0.78^[15a]) and hot-embossed films using mutual parallel patterns (S_{2D} Rust et al. = 0.85^[15a]). Additionally, other methods can reach comparable numbers S_{2D} Jintoku = 0.86.^[40] These measurements also reveal that the quality of alignment is substantial for both films and that there is little variation between the center and perimeter of the film. However, the slightly better alignment found on the CA patterned membrane, might be attributed to the more homogenous imprint or deformation of the pores, due to the evenly spread force during HE as discussed in Figure S1, Supporting Information.

Akin to the use of uniaxial aligned SWCNTs,^[11e,12a,14b] radially aligned SWCNT films could also find use in electronic devices and thus we performed two terminal electrical resistance measurements of a CA patterned film and compared this to an unaligned, random (RA) film. These measurements were made at sixteen equally spaced channels around the circumference of the film on an fPCB, Figure S9A, Supporting Information. A common ground (GND) pin was in the middle of the fPCB and slices were made with a sharp ceramic needle to separate the different elements, which were at an angle of 22.5° to their neighbors. The serial resistances stemming from the measurement setup comprising of an Arduino UNO, a multiplexer board, and Keithley multimeter were determined via a 100 Ω

reference resistance to be $\approx 60 \Omega$ and were thus subtracted from the measured values. The RA film was produced with identical mass, concentration, and filtration parameters as its aligned counterparts, but with an unmodified membrane. As expected, it can be seen that the average resistance of the radially aligned film is lower compared to its disordered counterpart $304 \pm 49 \Omega$ versus $478 \pm 93 \Omega$. Furthermore, the radial aligned film also had a lower standard deviation, indicating an improvement in consistency in resistance and thus leading to a more circular shape of resistances found at various angles of the film. In order to improve on these results, we speculate that the films would benefit even more from longer SWCNTs, as the intersection between individual SWCNTs is known to be the main contributor to resistance and larger SWCNTs have a higher charge carrier mobility as well.^[4]

3. Conclusion

In this work, the radial alignment of EA-SWCNTs has been demonstrated for the first time by HE PCTE membranes with custom-made shims and employing dead-end filtration. All but one pattern could be replicated by the filtered SWCNTs, with the exception being the herringbone pattern featuring a zig-zag line with alternating directions in the same length scale as the carbon nanotubes used, which indicates, that the alignment is dependent on a general shear flow rather than adhesion by charges. Additionally, we used Malu's law describing the films with a fixed and a rotating linear polarizer in order to define the normalized incident intensity I_0 as a new macroscopic order parameter yielding $I_{0,CA} = 0.82 \pm 0.02$ and $I_{0,SP} = 0.76 \pm 0.02$, and thus being in good agreement with large scale Raman mappings determining S_{2D} order parameters of 0.85 and 0.82 for the CA and SP patterns, respectively. Last, a simple terminal two probe resistance measurement was conducted between the middle of a CA film and radial contacts, showing a decrease of the resistance by one third compared to a disordered SWCNT film. These findings open the door to the fabrication of new SWCNT polarizers and might also include azimuthal and polarization converting elements^[42] in the future, surpassing conventional wire grids in terms of function and ease of use.

4. Experimental Section

Shim Production: The three different patterns for the master fabrication were designed with Klayout, Open Source, and converted into a machine-readable format by LayoutBEAMER Software from GenSYS. At first, a baking step (180 °C for 120 s) followed by an adhesion layer (Ti prime) was done on a standard non-oxidized 4" silicon wafer. A PMMA resist (AR-P 672.045; Allresist GmbH) was spin-coated at 3000 rpm for 60 s to a resist height of 100 nm followed by a second baking step (180 °C for 120 s). These substrates were used for structuring by electron beam lithography. The optimal dose of $2 \times 375 \mu\text{C cm}^{-2}$ results in structures with high quality and accuracy. After exposure, the nanostructures in PMMA were developed for 40 s in a solution of methyl isobutyl ketone and isopropyl alcohol (IPA) with a mixture ratio 1:3 by spray development. Layers of Chromium (≈ 7 nm) and gold (≈ 25 nm) were evaporated on top of the structured PMMA resist. The chromium layer serves as adhesive layer and the gold layer as conductive plating base for the subsequent electrodeposition

of nickel. During the evaporation step, the substrate was tilted at 30°. Nickel electroplating was performed within a standard electroforming electrolyte for ≈ 48 h, which contains boric acid and nickel sulphamate electrolyte as main components (working parameters pH 3.4 to 3.6 at 52 °C). For this, the metalized and structured master substrate was fixed by a commercial plating wafer holder (silicet AG, Lohfelden) and connected using a ring contact. To ensure a slow growth of the nickel layer (in the beginning of the electrodeposition) and to achieve a defect-free filling of the nanostructured areas the current density was adjusted at first to 0.1 A dm^{-2} (corresponding a growth speed of $\approx 0.02 \mu\text{m min}^{-1}$). Defect-free filling means the uniform growth of the electrochemically (galvanically) deposited nickel layer and the prevention of pores, holes, or inclusions within the lithographically fabricated nanostructures in the master. After 60 min, the current density was increased to 0.25 A dm^{-2} ($\approx 0.05 \mu\text{m min}^{-1}$) and in further steps up to 1.0 A dm^{-2} ($\approx 0.2 \mu\text{m min}^{-1}$). If a nickel layer thickness of at least 500 μm was generated, the plating process was stopped. The nickel shim was separated using a simple lift-off process. Subsequently, the resist was stripped with acetone (60 s) and the shim was cleaned with IPA (60 s, shaker). Both metallization layers (gold and chromium) were not etched and remain on the surface of the nickel shim. Finally, the shim has an outer diameter of 94 mm, a thickness of 500 μm , and structured area in the center with a diameter of 25 mm.

Filtration of Films: SWCNT thin films were produced with a custom-made microfluidic dead-end filtration setup, using large diameter (≈ 1.4 nm) EA-SWCNTs with a length of ($l = 691 \pm 471$ nm). The SWCNTs used in this work were well individualized and come from the same stock solution used in the work of Rust et al.,^[15a] which includes further details on the preparation and the constitution of the dispersions. The concentration of SWCNTs and DOC ($8 \mu\text{g mL}^{-1}$, 0.04 wt% DOC) as well as the filtration parameters ($100 \mu\text{L min}^{-1}$ ($J = 0.26 \text{ mm min}^{-1}$) for 1.25 mL and $500 \mu\text{L min}^{-1}$ ($J = 1.31 \text{ mm min}^{-1}$) for the remaining 0.75 mL) were consistent for all films. PVP-coated PCTE membranes were purchased from it4ip (batch resistance R2) with a diameter of 47 mm, pore size of 80 nm, a pore density of $6 \times 10^8 \text{ cm}^{-2}$, and a thickness of 25 μm .

Hot Embossing: The structures present on the shims were replicated on the membranes using a repurposed tensile test machine with attached heating capabilities and Pt-thermocouples.^[15a,37] All membranes regardless of the shim used, were hot-embossed at 120 °C at 20 kN for 10 min before cooling down to 40 °C (water circulation cooling) and lifting the load.

Film Transfer: After filtration, the membranes were wetted with deionized water (18.2 M Ω cm, pH = 6.93 from an Arium pro UV (Sartorius)) and adhered to the substrate with SWCNT film facing down. Subsequently, the films were slightly dried on a hot plate at 50 °C to remove most of the moisture before dissolving the membrane with Chloroform (99.2% stabilized with 0.6% ethanol, VWR Chemicals). This was achieved by placing the substrates with the film facing toward the bottom of a Petri dish and carefully raising the Chloroform levels until it reaches the membrane. As shown in Figure S10, Supporting Information, a small retaining device for the fPCBs was used to keep the polyimide taut during this process and avoid bubbles/rupturing of the SWCNT film. The fPCBs were custom designed using open source software KiCad EDA 5.1.12 and ordered at Multi Leiterplatten GmbH (Polyimide, contacts made of gold).

Atomic Force Microscopy: Imaging was performed using standard tapping mode in air with a Dimension Icon, Bruker (NSC 19 cantilevers, resonance frequency of 65 kHz, and a force constant of 0.5 Nm^{-1} (μmasch)) at a resolution of 256 lines. Topographies were 1. order flattened and leveled by the lowest measurement point using open-source Gwyddion.

Scanning Electron Microscopy: SWCNT films were imaged with a Zeiss Ultra Plus with a 30 μm aperture and an acceleration voltage of 2 kV.

Spectroscopy: Cross-polarized transmission measurements with linearly structured light and transmission measurements with azimuthal and radial beam profiles were performed with a supercontinuum laser (NKT-FIU15) at 650 nm at an initial power of 0.1 mW. A linear polarized light field was obtained by placing a linear polarizer after the laser, while the structured light beams were formed by an additional Q-plate

(ARCOptix). To form the structured light profiles, linearly polarized light polarized perpendicularly from the beam path, vertically for azimuthally polarized light, and horizontally for radially polarized light, were passed through the Q-plate. The beam then travels through two achromic, convex lenses from Edmund Optics to expand the beam in order to fill the SP and CA films. The beam after the film was then shrunk with two more achromatic lenses with the beam intensity recorded with a beam profiler from Thorlabs (BC106N). A schematic of the measurement setup is displayed in Figure S5, Supporting Information. The beam power (measured with a PM100d power meter and S121C photodiode power sensor from Thorlabs) just before the film was 9.1 μ W. Passing the beam through glass with no film, the registered power fell to 8.2 μ W.

A Horiba Xplora spectrometer equipped with a 2.33 eV laser source was used for the quantification via Raman measurements. The laser was focused on the aligned nanotubes with a $100\times$ (0.95 N.A.) objective using a laser power was 100 μ W. The backscattered light was collected with the same objective, dispersed by 1200 grooves per mm grating, and detected by a Silicon charge coupled device. The polarization was rotated perpendicular or parallel to the alignment direction by a built-in half-wave plate. In a similar manner, the analyzer was set for the desired direction. The 2D order parameter S_{2D} was calculated, using the following equation:^[17c]

$$S_{2D} = \frac{\Delta I_{VV} - I_{HH}}{\Delta I_{VV} + I_{HH} + (1 + \Delta) I_{VH}} \quad (1)$$

where I_{XY} indicates the G mode intensity (integrated area of the peak) with the incident light polarized along X and analyzer oriented toward Y. X and Y can take either V or H values, parallel or perpendicular to the orientation of the SWCNTs inside the film respectively. Δ_{UV} 532nm was the optical dichroic ratio at 532 nm, measured to be 1.55 for EA-SWCNT.^[15a] I_{HH} , I_{VV} , and I_{VH} was measured at every of the lateral position in a $24 \times 24 \mu\text{m}$ map, with 2 μm sampling. Benzonitrile molecules were used to calibrate for the different sensitivity in vertical and horizontal directions.

Cross-Polarized Light Microscopy: Scanning cross-polarized light microscopy was performed with a Leica DM6 M in reflectance mode for SWCNT films transferred to a glass slide. Rotation of the film was achieved with an optical rotation stage turned by 10° for every image. The contrast and brightness settings were identical for all films.

Two-Probe Resistance Measurements: The fPCBs were connected to a multiplexer (Analog Digital, 16 channels, SparkFun electronics) controlled by an Arduino Micro and the resistances were measured by a Keithley 2400 Standard Series SMU. In order to ensure a good contact the SWCNTs interfacing the gold contacts were slightly covered with liquid silver paste (Leitsilber 200N, Hans Wolbring GmbH). The resistance of the measurement setup was determined with a reference resistance to be $\approx 60 \Omega$.

Supporting Information

Supporting Information is available from the Wiley Online Library or from the author.

Acknowledgements

C.R. and E.S. contributed equally to this work. C.R., H.L., and B.S.F. gratefully acknowledge support from the Deutsche Forschungsgemeinschaft (DFG) under grant numbers FL 834/5-1, FL 834/7-1, FL 834/9-1, and FL 834/12-1. C.R. would also like to thank Marc Schneider for assistance with hot-embossing of the membranes. This work was partly carried out with the support of the Karlsruhe Nano Micro Facility, a Helmholtz Research Infrastructure at Karlsruhe Institute of Technology.

Open access funding enabled and organized by Projekt DEAL.

Conflict of Interest

The authors declare no conflict of interest.

Data Availability Statement

The data that support the findings of this study are available from the corresponding author upon reasonable request.

Keywords

1D crystals, hot-embossing, membranes, optical limiters, polarizers, terahertz spectroscopy, thin films

Received: December 8, 2022

Revised: January 25, 2023

Published online: February 12, 2023

- [1] L. Wieland, H. Li, C. Rust, J. Chen, B. S. Flavel, *Adv. Energy Mater.* **2021**, *11*, 2002880.
- [2] L. Sun, X. Wang, Y. Wang, Q. Zhang, *Carbon* **2017**, *122*, 462.
- [3] Z. Wu, Z. Chen, X. Du, J. M. Logan, J. Sippel, M. Nikolou, K. Kamaras, J. R. Reynolds, D. B. Tanner, A. F. Hebard, A. G. Rinzler, *Science* **2004**, *305*, 1273.
- [4] S. Matano, H. Takahashi, N. Komatsu, Y. Shimura, K. Nakagawa, J. Kono, H. Maki, *ACS Mater. Lett.* **2022**, *4*, 626.
- [5] a) A. Jorio, G. Dresselhaus, M. S. Dresselhaus, *Carbon Nanotubes: Advanced Topics in the Synthesis, Structure, Properties and Applications*, Springer, Berlin **2008**; b) M. S. Dresselhaus, G. Dresselhaus, A. Jorio, *Annu. Rev. Mater. Res.* **2004**, *34*, 247; c) R. Saito, G. Dresselhaus, M. S. Dresselhaus, *Physical Properties of Carbon Nanotubes*, Imperial College, London **1998**; d) M. Pfohl, D. D. Tune, A. Graf, J. Zaumseil, R. Krupke, B. S. Flavel, *ACS Omega* **2017**, *2*, 1163.
- [6] L. Wieland, H. Li, C. Rust, J. Chen, B. Flavel, *Adv. Energy Mater.* **2021**, *11*, 2170014.
- [7] X. Sun, T. Chen, Z. Yang, H. Peng, *Acc. Chem. Res.* **2013**, *46*, 539.
- [8] a) D. Wang, P. C. Song, C. H. Liu, W. Wu, S. S. Fan, *Nanotechnology* **2008**, *19*, 075609; b) S. J. Kang, C. Kocabas, T. Ozel, M. Shim, N. Pimparkar, M. A. Alam, S. V. Rotkin, J. A. Rogers, *Nat. Nanotechnol.* **2007**, *2*, 230; c) A. Ismach, D. Kantorovich, E. Joselevich, *J. Am. Chem. Soc.* **2005**, *127*, 11554.
- [9] C. Y. Khripin, X. Tu, J. M. Heddleston, C. Silvera-Batista, A. R. Hight Walker, J. Fagan, M. Zheng, *Anal. Chem.* **2013**, *85*, 1382.
- [10] Y. Feng, G. Zhou, G. Wang, M. Qu, Z. Yu, *Chem. Phys. Lett.* **2003**, *375*, 645.
- [11] a) G. Giancane, A. Ruland, V. Sgobba, D. Manno, A. Serra, G. M. Farinola, O. H. Omar, D. M. Guldj, L. Valli, *Adv. Funct. Mater.* **2010**, *20*, 2481; b) Q. Cao, S. J. Han, G. S. Tulevski, Y. Zhu, D. D. Lu, W. Haensch, *Nat. Nanotechnol.* **2013**, *8*, 180; c) H. Li, T. C. Hain, A. Muzha, F. Schoppler, T. Hertel, *ACS Nano* **2014**, *8*, 6417; d) G. J. Brady, Y. Joo, S. S. Roy, P. Gopalan, M. S. Arnold, *Appl. Phys. Lett.* **2014**, *104*, 083107; e) Y. Joo, G. J. Brady, C. Kanimozhi, J. Ko, M. J. Shea, M. T. Strand, M. S. Arnold, P. Gopalan, *ACS Appl. Mater. Interfaces* **2017**, *9*, 28859; f) H. Li, G. Gordeev, O. Garrity, S. Reich, B. S. Flavel, *ACS Nano* **2019**, *13*, 2567.
- [12] a) G. L. Goh, S. Agarwala, W. Y. Yeong, *ACS Appl. Mater. Interfaces* **2019**, *11*, 43719; b) X.-L. Xie, Y.-W. Mai, X.-P. Zhou, *Mater. Sci. Eng., R* **2005**, *49*, 89.
- [13] a) X. Li, Y. Jung, K. Sakimoto, T.-H. Goh, M. A. Reed, A. D. Taylor, *Energy Environ. Sci.* **2013**, *6*, 879; b) D. D. Tune, A. J. Blanch, C. J. Shearer, K. E. Moore, M. Pfohl, J. G. Shapter, B. S. Flavel,

- ACS Appl. Mater. Interfaces **2015**, *7*, 25857; c) C. Zamora-Ledezma, C. Blanc, M. Maughey, C. Zakri, P. Poulin, E. Anglaret, *Nano Lett.* **2008**, *8*, 4103.
- [14] a) K. R. Jinkins, J. Chan, G. J. Brady, K. K. Gronski, P. Gopalan, H. T. Evensen, A. Berson, M. S. Arnold, *Langmuir* **2017**, *33*, 13407; b) K. R. Jinkins, S. M. Foradori, V. Saraswat, R. M. Jacobberger, J. H. Dwyer, P. Gopalan, A. Berson, M. S. Arnold, *Sci. Adv.* **2021**, *7*, eabh0640.
- [15] a) C. Rust, H. Li, G. Gordeev, M. Spari, M. Guttman, Q. Jin, S. Reich, B. S. Flavel, *Adv. Funct. Mater.* **2022**, *32*, 2107411; b) J. S. Walker, J. A. Fagan, A. J. Biacchi, V. A. Kuehl, T. A. Searles, A. R. Hight Walker, W. D. Rice, *Nano Lett.* **2019**, *19*, 7256; c) X. W. He, W. L. Gao, L. J. Xie, B. Li, Q. Zhang, S. D. Lei, J. M. Robinson, E. H. Haroz, S. K. Doorn, W. P. Wang, R. Vajtai, P. M. Ajayan, W. W. Adams, R. H. Hauge, J. Kono, *Nat. Nanotechnol.* **2016**, *11*, 633.
- [16] a) R. Hu, G. Zhao, Y. He, H. Zhu, *Desalination* **2020**, *477*, 114271; b) Y. Ju, J. Zhang, Q. Cai, Z. Zhang, Y. Zhao, J. Cui, R. Hou, Y. Wei, Z. Liang, F. Chen, *Chem. Eng. J.* **2023**, *453*, 139969; c) J. Kang, Y. Choi, J. P. Kim, J. H. Kim, J. Y. Kim, O. Kwon, D. I. Kim, D. W. Kim, *J. Membr. Sci.* **2021**, *637*, 119620.
- [17] B. Dan, A. W. K. Ma, E. H. Házor, J. Kono, M. Pasquali, *Ind. Eng. Chem. Res.* **2012**, *51*, 10232.
- [18] B. King, B. Panchapakesan, *Nanotechnology* **2014**, *25*, 175201.
- [19] J. P. F. Lagerwall, G. Scalia, *J. Mater. Chem.* **2008**, *18*, 2890.
- [20] J. S. Walker, Z. J. Macdermid, J. A. Fagan, A. Kolmakov, A. J. Biacchi, T. A. Searles, A. R. H. Walker, W. D. Rice, *Small* **2022**, *18*, 2105619.
- [21] N. Komatsu, M. Nakamura, S. Ghosh, D. Kim, H. Chen, A. Katagiri, Y. Yomogida, W. Gao, K. Yanagi, J. Kono, *Nano Lett.* **2020**, *20*, 2332.
- [22] L. Ren, C. L. Pint, T. Arikawa, K. Takeya, I. Kawayama, M. Tonouchi, R. H. Hauge, J. Kono, *Nano Lett.* **2012**, *12*, 787.
- [23] a) P. Yeh, *Opt. Commun.* **1978**, *26*, 289; b) S.-W. Ahn, K.-D. Lee, J.-S. Kim, S. H. Kim, J.-D. Park, S.-H. Lee, P.-W. Yoon, *Nanotechnology* **2005**, *16*, 1874.
- [24] K. Wiesauer, C. Jördens, *J. Infrared, Millimeter, Terahertz Waves* **2013**, *34*, 663.
- [25] A. Baydin, N. Komatsu, F. Tay, S. Ghosh, T. Makihara, G. T. Noe, J. Kono, *Optica* **2021**, *8*, 760.
- [26] Y. Hou, Y. Jung, *AIP Adv.* **2022**, *12*, 065023.
- [27] a) N. Friedman, A. Kaplan, N. Davidson, *Adv. At., Mol., Opt. Phys.* **2002**, *48*, 99; b) B. Feng, E. Liu, Z. Wang, W. Cai, H. Liu, S. Wang, T. Liang, W. Xiao, J. Liu, *Appl. Phys. Express* **2016**, *9*, 062003.
- [28] E. A. Nanni, W. R. Huang, K.-H. Hong, K. Ravi, A. Fallahi, G. Moriena, R. Dwayne Miller, F. X. Kärtner, *Nat. Commun.* **2015**, *6*, 8486.
- [29] D. Schulz, B. Schwager, J. Berakdar, *ACS Photonics* **2022**, *9*, 1248.
- [30] T. Watanabe, Y. Iketaki, T. Omatsu, K. Yamamoto, M. Sakai, M. Fujii, *Opt. Express* **2003**, *11*, 3271.
- [31] B. Sick, B. Hecht, L. Novotny, *Phys. Rev. Lett.* **2000**, *85*, 4482.
- [32] Y. Chen, Y. Lin, Y. Liu, J. Doyle, N. He, X. Zhuang, J. Bai, W. J. Blau, *J. Nanosci. Nanotechnol.* **2007**, *7*, 1268.
- [33] V. M. Gubarev, V. Y. Yakovlev, M. G. Sertsu, O. F. Yakushev, V. M. Krivtsun, Y. G. Gladush, I. A. Ostanin, A. Sokolov, F. Schäfers, V. V. Medvedev, A. G. Nasibulin, *Carbon* **2019**, *155*, 734.
- [34] W. Yu, C. Liu, S. Fan, *Nano Res.* **2021**, *14*, 2471.
- [35] P. Arenas-Guerrero, M. L. Jiménez, K. Scott, K. J. Donovan, *Carbon* **2018**, *126*, 77.
- [36] W. P. S. Freitas, C. R. Cena, D. C. B. Alves, A. M. B. Goncalves, *Phys. Educ.* **2018**, *53*, 035034.
- [37] a) W. Zou, J. Sackmann, A. Striegel, M. Worgull, W. K. Schomburg, *Microsyst. Technol.* **2019**, *25*, 4185; b) A. Díaz Lantada, N. Mazarío Picazo, M. Guttman, M. Wissmann, M. Schneider, M. Worgull, S. Hengsbach, F. Rupp, K. Bade, G. R. Plaza, *Materials* **2020**, *13*, 1586.
- [38] a) V. G. J. Rodgers, R. E. Sparks, *J. Membr. Sci.* **1992**, *68*, 149; b) K. Nakamura, T. Orime, K. Matsumoto, *J. Membr. Sci.* **2012**, *401–402*, 274.
- [39] C. Rust, P. Shapturenka, M. Spari, Q. Jin, H. Li, A. Bacher, M. Guttman, M. Zheng, T. Adel, A. R. H. Walker, J. A. Fagan, B. S. Flavel, *Small* **2022**, 2206774.
- [40] H. Jintoku, Y. Matsuzawa, *ACS Appl. Nano Mater.* **2022**, *5*, 2195.
- [41] M. Brohmann, F. J. Berger, M. Matthiesen, S. P. Schießl, S. Schneider, J. Zaumseil, *ACS Nano* **2019**, *13*, 7323.
- [42] A. Mehta, J. D. Brown, P. Srinivasan, R. C. Rumpf, E. G. Johnson, *Opt. Lett.* **2007**, *32*, 1935.